

1 Supporting Information for

2 Product distribution, kinetics, and aerosol formation from the 3 OH oxidation of dimethyl sulfide under different RO₂ regimes

4 Qing Ye^{1*}, Matthew B. Goss¹, Jordan E. Krechmer², Francesca Majluf², Alexander Zaytsev³,
5 Yaowei Li³, Joseph R. Roscioli⁴, Manjula Canagaratna², Frank N. Keutsch^{3,5}, Colette L. Heald¹
6 and Jesse H. Kroll¹

7 ¹Department of Civil and Environmental Engineering, Massachusetts Institute of Technology,
8 Cambridge, Massachusetts 02139, United States

9 ²Center for Aerosol and Cloud Chemistry, Aerodyne Research Incorporated, Billerica,
10 Massachusetts 01821, United States

11 ³John A. Paulson School of Engineering and Applied Sciences, Harvard University, Cambridge,
12 Massachusetts 02138, United States

13 ⁴Center for Atmospheric and Environmental Chemistry, Aerodyne Research Incorporated,
14 Billerica, Massachusetts 01821, United States

15 ⁵Department of Chemistry and Chemical Biology, Department of Earth and Planetary Sciences,
16 Harvard University, Cambridge, Massachusetts 02138, United States

17 *Now at the Atmospheric Chemistry Observations and Modeling Laboratory, National Center for
18 Atmospheric Research, Boulder, Colorado 80301, United States

19 Correspondence to: Qing Ye (qingye@ucar.edu), Jesse H. Kroll (jhkroll@mit.edu)

20 21 1. Reaction mechanisms used in the box model

22 The full DMS + OH reaction scheme used in the box model is presented in Figure 1. Reactions
23 added to the default sulfur chemistry currently in MCMv3.3.1 are given in Table S1.

24
25 **Table S1: Reactions added to the default sulfur chemistry in MCMv3.3.1. (Jenkin et al., 1997;
26 Saunders et al., 2003) in the box model**

Gas-phase reactions	k^a	References
$\text{CH}_3\text{SCH}_2\text{OO} \rightarrow \text{OOCH}_2\text{SCH}_2\text{OOH}$ (isomerization)	0.09	Ye <i>et al.</i> 2021
$\text{OOCH}_2\text{SCH}_2\text{OOH} \rightarrow \text{HOOCH}_2\text{SCHO} + \text{OH}$	$5.8 \times 10^{11} \exp(-10155/T + 1080200/T^2)$	Wu <i>et al.</i> 2015
$\text{OOCH}_2\text{SCH}_2\text{OOH} + \text{NO} \rightarrow \text{OCH}_2\text{SCH}_2\text{OOH} + \text{NO}_2$	$4.9 \times 10^{-12} \exp(260/T)$	Same as $\text{CH}_3\text{SCH}_2\text{OO}$ in MCMv3.3.1
$\text{OOCH}_2\text{SCH}_2\text{OOH} + \text{HO}_2 \rightarrow \text{HOOCH}_2\text{SCH}_2\text{OOH}$	$1.13 \times 10^{-12} \exp(1300/T)$	Same as $\text{CH}_3\text{SCH}_2\text{OO}$ in MCMv3.3.1
$\text{OCH}_2\text{SCH}_2\text{OOH} \rightarrow \text{SCH}_2\text{OOH} + \text{HCHO}$	1×10^6	Same as $\text{CH}_3\text{SCH}_2\text{O}$ in MCMv3.3.1
$\text{HOOCH}_2\text{SCHO} + \text{OH} \rightarrow \text{HOOCH}_2\text{SCO}$	1.0×10^{-11}	Vermeuel <i>et al.</i> 2020

$\text{HOOCH}_2\text{SCO} \rightarrow \text{CO} + \text{HOOCH}_2\text{S}$	$9.2 \times 10^9 \exp(-505.4/T)$	Wu <i>et al.</i> 2015
$\text{HOOCH}_2\text{SCO} \rightarrow \text{OH} + \text{HCHO} + \text{OCS}$	$1.6 \times 10^7 \exp(-1468.6/T)$	Wu <i>et al.</i> 2015
$\text{HOOCH}_2\text{S} + \text{NO}_2 \rightarrow \text{HOOCH}_2\text{SO} + \text{NO}$	$6.0 \times 10^{-11} \exp(240/T)$	Same as CH_3S in MCMv3.3.1
$\text{HOOCH}_2\text{S} + \text{O}_3 \rightarrow \text{HOOCH}_2\text{SO} + \text{O}_2$	$1.15 \times 10^{-12} \exp(430/T)$	Same as CH_3S in MCMv3.3.1
$\text{HOOCH}_2\text{SO} + \text{O}_3 \rightarrow \text{SO}_2 + \text{HCHO} + \text{OH} + \text{O}_2$	4.0×10^{-13}	Same as CH_3SO in MCMv3.3.1
$\text{HOOCH}_2\text{SO} + \text{NO}_2 \rightarrow \text{SO}_2 + \text{HCHO} + \text{OH} + \text{NO}$	1.2×10^{-11}	Same as CH_3SO in MCMv3.3.1

a: The units of k are s^{-1} for unimolecular reactions and $\text{cm}^3 \text{ molec}^{-1} \text{ s}^{-1}$ for bimolecular reactions.

2. Instruments

Table S2: S-containing products detected and the corresponding instruments

Formula detected (not including primary ions)	Assigned species	Vocus PTR-MS	I ⁻ -CIMS	NH ₄ ⁺ -CIMS	AMS	Compact TILDAS
C ₂ H ₆ S	Dimethyl sulfide	✓				
C ₂ H ₆ SO	Dimethyl sulfoxide	✓		✓		
C ₂ H ₆ SO ₂	Dimethyl sulfone, Methylthiomethyl hydroperoxide	✓		✓		
C ₂ H ₄ SO	Methylthioformate	✓		✓		
CH ₄ SO ₂	Methanesulfinic acid	✓	✓	✓		
C ₂ H ₄ SO ₃	Hydroperoxymethyl thioformate		✓	✓		
CH ₃ SO ₆ N	Methanesulfonyl peroxy nitrate		✓			
CH ₂ SO ₂	Thioacid		✓			
CH ₃ SO ₂ ⁺ etc	Methane sulfonic acid				✓	
SO ⁺ , SO ₂ ⁺ , SO ₃ ⁺ etc	Sulfuric acid/Sulfate aerosol				✓	
	Sulfur dioxide					✓

2.1 Vocus PTR-MS measurements

A Vocus Proton-Transfer-Reaction Time-of-Flight Mass Spectrometer (Vocus PTR-MS, Aerodyne Research Inc.) was used to measure the precursor and lightly oxygenated products from the oxidation (see Table S1) with sub-ppt detection limits (Krechmer *et al.*, 2018). The instrument details are documented in Krechmer *et al.* (Krechmer *et al.*, 2018). Reaction mixtures were directly sampled from the chamber at 1 slpm and measured at 1 Hz frequency. The compounds in the mixtures were ionized by proton transfer reactions with the hydronium ion (H₃O⁺) and detected as M•H⁺.

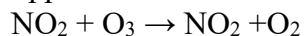
41 The sensitivity of the Vocus PTR-MS to a wide range of compounds was calibrated using two
42 methods. In the first method, the instrument sampled a flow of calibration gas from a cylinder that
43 contained 5 ppb of an array of compounds including acetone, benzene, α -pinene and several other
44 VOCs. This calibration was performed every 4 hours during the experiments. In the second
45 calibration, a liquid calibration system was used to generate known amounts of species that were
46 expected to form in the experiments including DMSO and DMSO_2 , by quantitatively evaporating
47 the solution containing the compounds of known concentrations into a stream of ultra-zero gas that
48 was sampled by the instrument. By varying the concentration of the solution, a four-point
49 calibration was conducted, denoted as the reference sensitivity for DMSO and DMSO_2 , $S_{\text{DMSO_ref}}$
50 and $S_{\text{DMSO}_2\text{-ref}}$. The second type of calibration was conducted two times during the middle of the
51 chamber campaign, and the sensitivities to DMSO and DMSO_2 were averaged between the two
52 calibrations. The sensitivity uncertainty of DMSO and DMSO_2 was determined to be 10% and 3%,
53 respectively, by taking the standard deviation of the sensitivities derived from the two calibrations.
54 Acetone sensitivity using the calibration gas was also calibrated during the second calibration,
55 denoted as $S_{\text{acetone_ref}}$. The instrument sensitivity may vary over time, and therefore, the sensitivity
56 of DMSO (and similarly DMSO_2) in every experiment was derived by scaling the acetone
57 reference sensitivity:

$$S_{\text{DMSO_exp}} = S_{\text{DMSO_ref}} \times \frac{S_{\text{acetone_exp}}}{S_{\text{acetone_ref}}}.$$

60 2.2 I⁻-CIMS measurements

61 An Iodide Time-of-Flight Chemical Ionization Mass Spectrometer (I⁻-CIMS) was used to measure
62 more oxidized species in the reaction mixture. A ²¹⁰Po strip (10 mCi, NRD LLC) was used to
63 ionize methyl iodide vapor from a permeation tube forming I⁻ as the reagent ions. A 1.8 slpm
64 sample flow taken from the chamber was mixed with a 2 slpm humidified N₂ flow carrying the
65 reagent ions in the ion-molecule reactor.

66 To calibrate and constrain the sensitivity of the I⁻-CIMS to a broad range of compounds including
67 products in DMS oxidation, calibrations using authentic standards and the voltage scanning
68 technique (Isaacman-Vanwertz et al., 2018; Lopez-Hilfiker et al., 2016) were used. First, the
69 sensitivity of N₂O₅ which represents the maximum sensitivity of the instrument was determined.
70 A known amount of N₂O₅ was formed in the chamber under dry condition by injecting 1-5 ppb of
71 O₃ into the chamber prefilled with 1-2 ppm of NO₂:



72 Each addition of O₃ was allowed to equilibrate until the N₂O₅•I⁻ signal was stable. The total
73 measured signals of N₂O₅ by the I⁻-CIMS included N₂O₅I⁻ and NO₃⁻ ions (Lopez-Hilfiker et al.,
74 2016). Multiple O₃ additions were conducted to derive a multi-point calibration, and the N₂O₅
75 concentration in the chamber was calculated using the F0AM model. The derived N₂O₅ sensitivity
76 is 12 cps ppt⁻¹ (normalized to 10⁶ cps reagent ions).

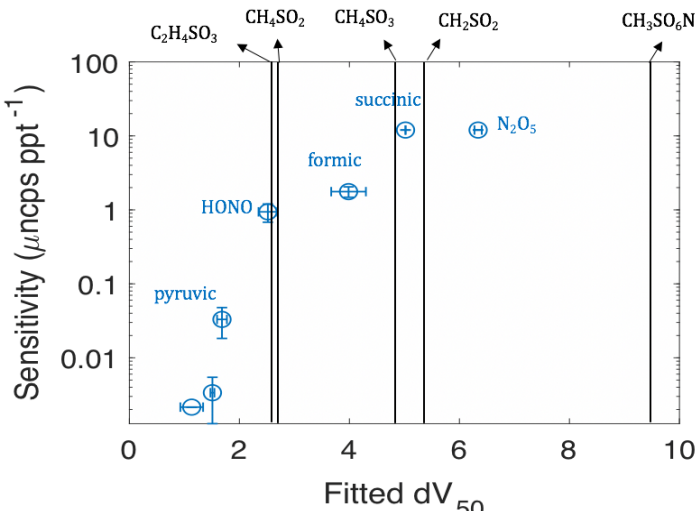
77 The sensitivities of several organic acids were also calibrated by using the liquid calibration
78 system. Similar to the calibration of Vocus PTR-MS, known concentrations of calibrants were
79 delivered to the I⁻-CIMS for a multipoint calibration by quickly evaporating the solution containing
80 the calibrants in the liquid calibration system. Voltage scanning was performed during the
81 calibration by changing the voltage between the skimmer and big segment quadrupole to examine

86 the binding energy of the iodide-molecule adduct, denoted as dV50, the voltage at which 50% of
87 the adduct declustered (Isaacman-Vanwertz et al., 2018; Lopez-Hilfiker et al., 2016).

88
89 Figure S2 shows the relationship between the measured sensitivity and dV50 for compounds
90 calibrated. It is known that succinic acid is measured close to the maximum instrument sensitivity⁶
91 and therefore, it is determined that species with a dV50 ~5V or greater will be detected at the
92 maximum sensitivity. Voltage scanning was also performed every two hours in every experiment
93 for all species measured. Based on the voltage scanning results, the sensitivities of sulfur-
94 containing products were estimated: dV50 for CH_4SO_3 (MSA), CH_2SO_2 (thioacid or sulfene) and
95 $\text{CH}_3\text{SO}_6\text{N}$ (methanesulfonyl peroxy nitrate) were 4.7 V, 5.4 V and 9.4 V, respectively; their
96 sensitivities were therefore estimated to be 12 cps ppt⁻¹. The dV50 for $\text{C}_2\text{H}_4\text{SO}_3$ (HPMTF) and
97 CH_4SO_2 (MISA) were 2.6 V and 2.7 V, respectively, close to the dV50 of HONO, and their
98 sensitivities were estimated to be the same as HONO, 1.0 cps ppt⁻¹.

99
100 There are substantial uncertainties for the estimated sensitivities using voltage scanning.
101 Therefore, in Section 3.3 in which the yield of HPMTF was calculated to derive the isomerization
102 rate coefficient (k_{isom}) of the $\text{CH}_3\text{SCH}_2\text{OO}$ radical, a calibration factor was included (Eq. 1 and Eq.
103 4). However, the fitting in Figure 3(a) is only sensitive to the shape of the curve, and not the
104 absolute value. This helps minimize the effect of uncertainty of the HPMTF calibration on the
105 determination of k_{isom} . Note that in dry experiments, good sulfur closure measurements were
106 obtained from data collected by independently calibrated instruments, and the asymptote value in
107 Figure 2a is close to 1, suggesting that our estimated sensitivities were reasonable. To estimate
108 the overall uncertainty in the sulfur closure, a 50% relative standard deviation was applied to
109 individual species measured by the I-CIMS.

110



111
112 Figure S1: I-CIMS sensitivity of N_2O_5 and organic acids versus their iodide cluster disassociation voltage
113 derived from voltage scanning. The sensitivities of the sulfur-containing products are determined as the
114 following: $\text{SC}_2\text{H}_4\text{SO}_3 = 1 \text{ cps ppt}^{-1}$, $\text{SCH}_4\text{SO}_2 = 1 \text{ cps ppt}^{-1}$, $\text{SCH}_4\text{SO}_3 = 12 \text{ cps ppt}^{-1}$, $\text{SCH}_2\text{SO}_2 = 12 \text{ cps ppt}^{-1}$,
115 $\text{SCH}_3\text{SO}_6\text{N} = 12 \text{ cps ppt}^{-1}$, normalized to $10^6 \text{ cps reagent ions}$.

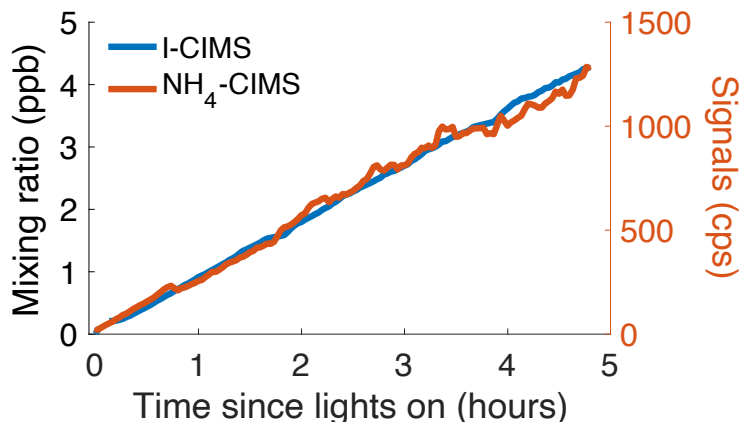
116

117 2.3 NH_4^+ -CIMS measurements

118 A time-of-flight chemical ionization mass spectrometer which used ammonium (NH_4^+) as the
119 reagent ion (NH_4^+ -CIMS) was also deployed to measured oxygenated products (Zaytsev et al.,
120 2019). Table S1 lists the sulfur-containing species by the NH_4^+ -CIMS. The instrument uses a $\frac{1}{4}$ "
121 PFA Teflon sampling line with a flow of 3.5 slpm. The instrument is designed to minimize inlet
122 losses of sampled compounds. The dominant reagent ions are $\text{NH}_4^+\bullet(\text{H}_2\text{O})_n$, ($n = 0, 1, 2$), and
123 chemical species are detected as ammonium-clusters $\text{NH}_4^+\bullet(\text{M})$ through ligand-switching
124 reactions.

125
126 Unlike the I-CIMS, the NH_4^+ -CIMS detects HPMTF without the interference from N_2O_5 . Figure
127 S3 illustrates that the $\text{C}_2\text{H}_4\text{SO}_3\text{-}^{12}\text{C}_2$ signal measured by both instruments show a consistent time
128 series in Exp. 2a. This confirms that there is negligible N_2O_5 interference in the I-CIMS
129 measurements of HPMTF used in the total-sulfur analysis.

130
131



132
133
134 Figure S2: Time series of $\text{C}_2\text{H}_4\text{SO}_3$ (from DMS- $^{12}\text{C}_2$) measured by the I-CIMS and the NH_4 -CIMS.

135
136 **2.4. Aerodyne Compact Tunable Infrared Laser Direct Absorption Spectrometer (TILDAS)**
137 The SO_2 concentration was measured using an Aerodyne Compact Tunable Infrared Laser Direct
138 Absorption Spectrometer (TILDAS) (McManus et al., 2011; McManus et al., 1995). The single-
139 laser instrument measured SO_2 absorptions near 1352 cm^{-1} , in a 76-m astigmatic multipass
140 absorption cell (AMAC) (McManus et al., 1995). The continuous wave laser was rapidly scanned
141 at kHz rates, and resulting spectra were averaged every second and fit on-the-fly using on board
142 software (TDLWintel). Typical 1-s noise levels were 160 ppt, averaging to < 40 ppt in 100
143 seconds. The instrument was zeroed every 5 minutes using ultra-zero air, and calibrated using a
144 5.1 ppm standard diluted into an ultra-zero air overflow from 0-1000 ppb.

145
146 **2.5 Particle-phase measurements using the aerosol mass spectrometer**
147 *Calibration and raw data analysis*
148 The aerosol mass spectrometer (AMS) was calibrated for ionization efficiency using ammonium
149 nitrate. Relative ionization efficiencies (RIE) for NH_4^+ (3.96), SO_4^{2-} (0.92), and MSA (1.20) were
150 calculated using NH_4NO_3 , NH_4SO_4 , and $\text{NH}_4(\text{CH}_3\text{SO}_3)$ using the ammonium balance method
151 (Hodshire et al., 2019).

152

153 Quantification of MSA was performed using SQUIRREL 1.63B and PIKA 1.23B based on the
154 method published by Huang *et al.*, 2017 (Huang et al., 2017), where the total mass of MSA is
155 based on a reference spectrum and the distinctive fragment CH_3SO_2^+ . Since MSA fragmentation
156 has been shown to vary based on instrumental factors (Zorn et al., 2008), a pure MSA spectrum
157 for our instrument was taken from MSA aerosolized into the chamber. The reference spectrum was
158 obtained by summing the high-resolution families that contribute to the MSA spectrum (CHOgt1,
159 CHO1, CH, CS, C_x, SO, HS) and removing others (such as NH) that result from trace ammonia in
160 the chamber/sampling lines. No significant ions except for CH_3SO_2^+ were observed at *m/z* 79 in
161 high resolution analysis during the experiments so the entire unit mass was assigned to this ion.
162 For Experiment 4 when the AMS was operated at 800 °C, a reference spectrum for MSA taken at
163 800 °C was used instead. The fragmentation table in SQUIRREL 1.63B was adjusted according to
164 the reference spectrum.

165
166 For experiments in which both ¹²C- and ¹³C-DMS were used, this method was modified to account
167 for both isotopes. A reference ¹³C-MSA spectrum was first derived from the ¹²C-MSA spectrum
168 by inspection—based on which ions contain carbon—since no pure sample is easily available.
169 Next, the ¹²C / ¹³C isotope ratio, which remained constant throughout each experiment, was derived
170 based on high resolution fitting at *m/z* 96 and *m/z* 97 where few ions interfered with the $\text{^{12}CH}_4\text{SO}_3^+$
171 and $\text{^{13}CH}_4\text{SO}_3^+$ signals. The key peak for ¹³C-MSA ($\text{^{13}CH}_3\text{SO}_2^+$) was easily distinguished from
172 SO_3^+ in high resolution and the ratio of these ions was used to calculate the total ¹³C-MSA mass
173 using the reference spectrum and the unit mass resolution frag table. The signal from the key peak
174 for ¹²C-MSA ($\text{^{12}CH}_3\text{SO}_2^+$) is estimated based on the ¹²C / ¹³C isotope ratio and the $\text{^{13}CH}_3\text{SO}_2^+$
175 signal; total ¹²C-MSA mass is then calculated as above based on the derived $\text{^{12}CH}_3\text{SO}_2^+$ signal.
176

177 *Corrections*

178 Particle wall loss was accounted for when estimating the concentration of aerosol-phase products.
179 Particle wall loss rate was expected to be faster during the beginning of the experiment and
180 gradually decreased as the experiment proceeds due to the growth of the particles. The estimate of
181 particle wall loss rate was performed by measuring the loss rate of particle containing 2:1 mix of
182 H_2SO_4 and MSA by aerosolizing the solution containing the mixture into the chamber. This particle
183 composition roughly matched that of the observed products. AMS results corrected by this single
184 mass-based wall loss rate coefficient were taken as the “best estimate”, which was $5.74 \times 10^{-5} \text{ s}^{-1}$,
185 and was applied for wall loss correction for entire experiments based on Wang *et al.* (Wang et al.,
186 2018). Upper ($1.59 \times 10^{-4} \text{ s}^{-1}$) and lower ($4.58 \times 10^{-5} \text{ s}^{-1}$) bounds for this wall loss correction were
187 additionally calculated based on the faster average loss rate of the NaNO_3 seed particles and the
188 slower average rate at the end of experimental particle losses, respectively. Particle mass
189 concentrations calculated using the upper and lower bounds of wall loss correction were included
190 in the overall uncertainty of the sulfur closure.
191

192 Additionally, due to the presence of some particles below the optimal AMS transmission size
193 range, a small correction to the total AMS mass was applied based on the SMPS size distribution
194 and the AMS transmission efficiency curve (Guo et al., 2021), under the assumption that these
195 particles had the same chemical composition. This was done by calculating and correcting for the
196 fraction of the SMPS signal that would not be detected by the AMS. This correction increased
197 calculated mass by an average of 2%. During high-RH experiments, a diffusion dryer was placed
198 upstream of aerosol measurements to remove effects of RH in particle quantifications. By

199 combining the AMS and SMPS data from experiments with a high aerosol yield, the AMS
 200 collection efficiency (CE) was estimated assuming spherical particles without voids. The CE for
 201 Exp. 1 was estimated to be ~ 0.5 , consistent with the previous DMS study published from our
 202 group (Ye et al., 2021). The CE for Exp. 4 was ~ 0.3 . The lower CE was probably due to the
 203 increased particle bounce caused by the sodium chloride seed particles. For the low-aerosol-yield
 204 experiments which used the same seed particles as in Exp. 1, a collection efficiency of 0.5 was
 205 applied.

207 3. Estimation of HPTMF vapor pressure and chamber wall loss

208 Currently there is no reported experimentally measured saturation vapor pressure of HPMTF,
 209 C_{HPMTF} , under room temperature. Here, C_{HPMTF} is estimated using two methods. In the first method,
 210 the pure component vapor pressure of HPMTF is estimated by based on Compernolle *et al.*
 211 (Compernolle et al., 2011) calculated by UManSysProp (<http://umansysprop.seaes.manchester.ac.uk/>). The estimated C_{HPMTF} is $\sim 1 \times 10^8 \mu\text{g m}^{-3}$. In the second method, C_{HPMTF} is estimated based
 212 on the vapor pressure of DMS which is $\sim 500 \text{ mmHg}$ at room temperature (NIST webBook). The
 213 addition of the aldehyde group and the hydroperoxide group are expected to lower the vapor
 214 pressure by ~ 1 and ~ 2.2 decades, respectively (Capouet and Muller, 2006; Pankow and Asher,
 215 2008). Thus, C_{HPMTF} is estimated to be on the order of $1 \times 10^6 \mu\text{g m}^{-3}$. Both methods suggest that
 216 C_{HPMTF} is at least two orders of magnitudes greater than the equivalent organic mass of the chamber
 217 wall, C_w , which is on the order of $1 \times 10^4 \mu\text{g m}^{-3}$ (Krechmer et al., 2016). Therefore, only a very
 218 small amount ($\sim 1\%$ or less) of HPTMF is expected to be deposited onto the chamber wall under
 219 dry condition.

222 4. Determination of k_{isom} of $\text{CH}_3\text{SCH}_2\text{OO}$

223 In Exp.3, the oxidation was initiated by H_2O_2 photolysis with 3 ppb of NO in the chamber. Later,
 224 different amounts of HONO or NO was injected into the chamber several times to perturb the
 225 chemistry of the RO_2 radicals, and in particular decreasing its τ_{bi} . Each perturbation lasted for ~ 10
 226 minutes, and the branching fraction of the $\text{CH}_3\text{SCH}_2\text{OO}$ radicals that undergo isomerization, f_{isom} ,
 227 was determined by using the yield of HPMTF in the abstraction channel from the measurements:

$$228 Y_{\text{HPMTF}} = f_{\text{isom}} = \frac{a_{\text{cal}} \times \Delta \text{HPMTF}}{\Delta \text{DMS} \times f_{\text{abs}}}. \quad \text{Eq. S1}$$

229 In Figure 2 in which the loss of HPMTF via OH oxidation is not considered, ΔHPMTF is simply
 230 the change in the measured HPMTF concentration, $\Delta \text{HPMTF}_{\text{meas}}$. When taking loss by OH
 231 oxidation into account, $\Delta \text{HPMTF} = \Delta \text{HPMTF}_{\text{meas}} + \int k_{\text{HPMTF+OH}} \times \Delta [\text{HPMTF}][\text{OH}] dt$. Here,
 232 $2.1 \times 10^{-11} \text{ cm}^3 \text{ molec}^{-1} \text{ s}^{-1}$ is used as $k_{\text{HPMTF+OH}}$ derived from our measurements.

233 f_{isom} is also determined by the rate coefficient of the isomerization channel and the bimolecular
 234 channels of the $\text{CH}_3\text{SCH}_2\text{OO}$ radical:

$$236 f_{\text{isom}} = \frac{k_{\text{isom}}}{k_{\text{isom}} + k_{\text{bi}}} \quad \text{Eq. S2}$$

237 Here, k_{bi} is the bimolecular rate of $\text{CH}_3\text{SCH}_2\text{OO}$ with HO_2 and NO, derived from

$$238 k_{\text{bi}} = \frac{1}{\tau_{\text{bi}}} = k_{\text{HO}_2}[\text{HO}_2] + k_{\text{NO}}[\text{NO}] \quad \text{Eq. S3}$$

239 Taken together, k_{isom} can be estimated by fitting the following equation from the perturbations:

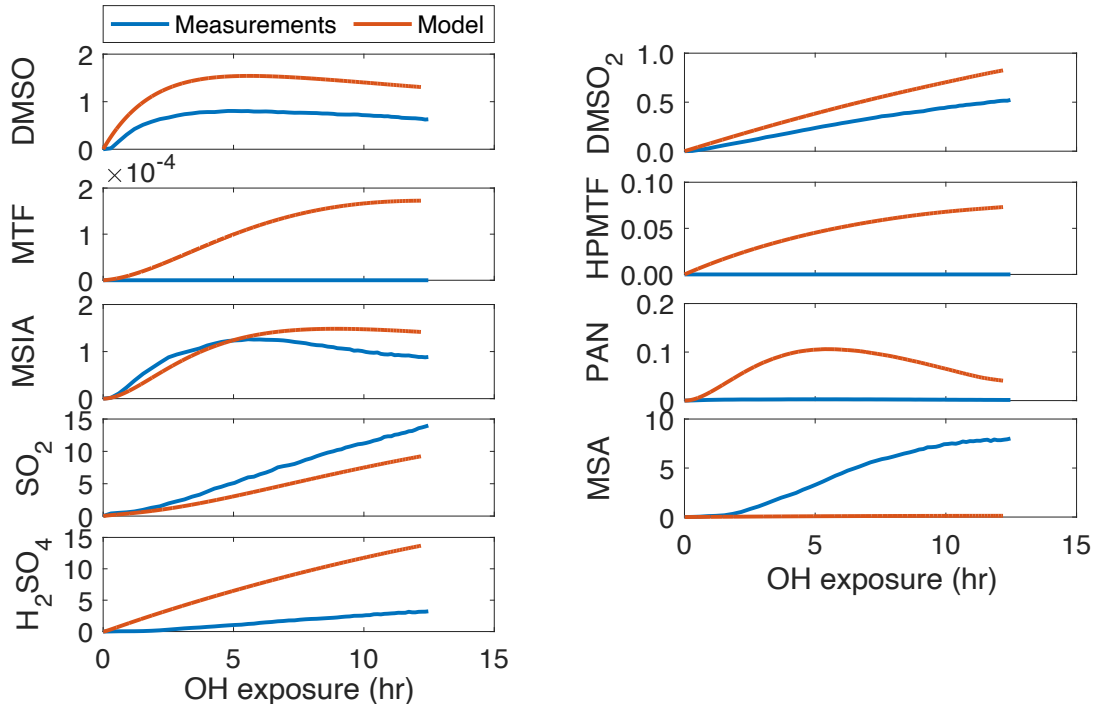
$$240 Y_{\text{HPMTF}} = \frac{1}{a_{\text{cal}}} \times \frac{k_{\text{isom}}}{k_{\text{isom}} + \frac{1}{\tau_{\text{bi}}}} \quad \text{Eq. S4}$$

241 Here, $f_{\text{abs}} = 0.65$, which is based on the branching fraction of the abstraction channel under the
 242 temperature in this work (Barnes et al., 2006). A calibration factor, a_{cal} , was included as a

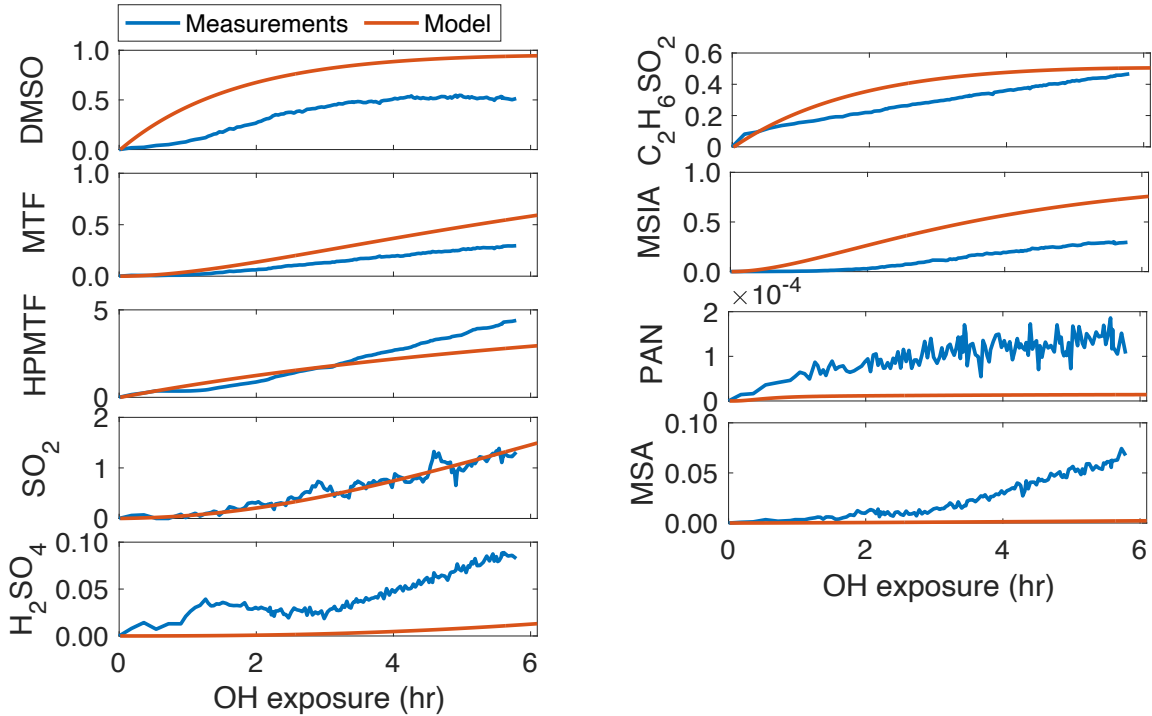
243 parameter to account for the calibration uncertainty of HPMTF in the measurements; however its
 244 value has negligible impacts on the inflection point of the fitted curve in Figure 2a. The initial
 245 concentration of NO in each perturbation was constrained by the measurements, and the
 246 subsequent change of NO was derived from F0AM simulations. $[\text{HO}_2]$ was also derived from
 247 F0AM simulations, and k_{HO_2} and k_{NO} were taken from MCM_V3.3.1 (Jenkin et al., 1997;
 248 Saunders et al., 2003). $[\text{NO}]$ and $[\text{HO}_2]$ were averaged for each of the 10-minute period.
 249

250 **5. Other supporting figures**

251
 252

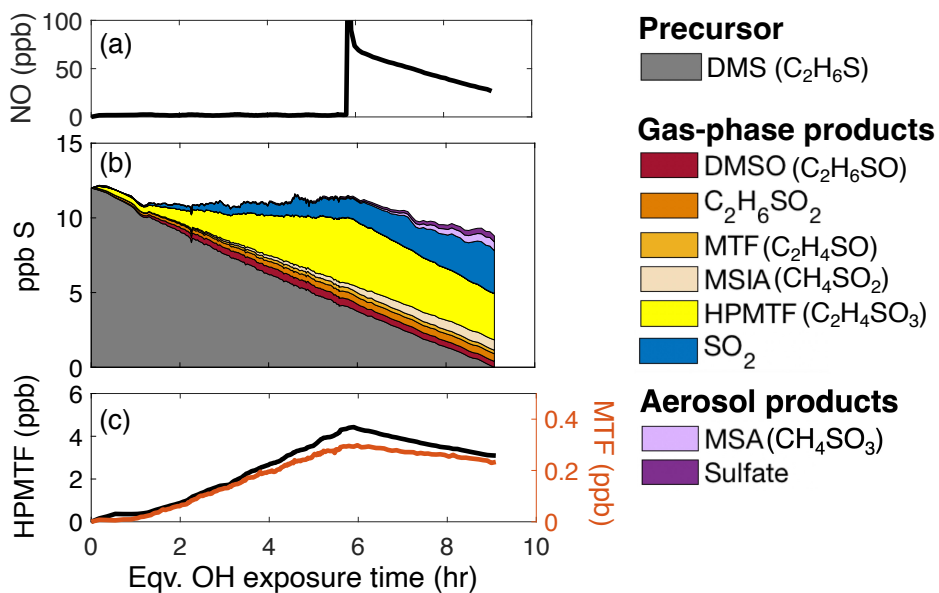


253
 254 Figure S3: Measurement-model comparison of individual sulfur-containing products under the high-NO
 255 condition (Experiment 1). Concentrations (y axis) are in ppb S.
 256
 257



258
259
260
261

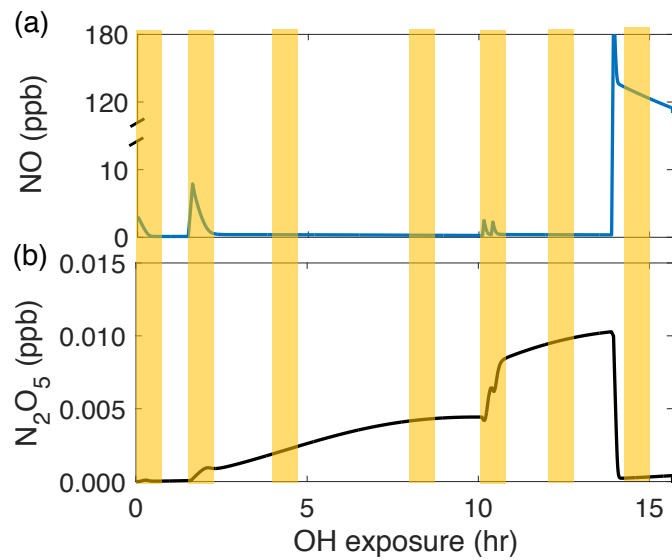
Figure S4: Measurement-model comparison of individual sulfur products under the low-NO condition (Exp. 2a). Concentrations (y axis) are in ppb S.



262
263
264
265
266
267
268
269

Figure S5: (a) NO concentration measured by the NO-NO₂-NO_x analyzer in Exp. 2a and 2b. At OH exposure ~ 5.8 h, 70 ppb of NO was injected into the chamber. (b) Total sulfur distribution in Experiment 2a and 2b. (c) Time series of HPMTF and MTF in Experiment 2 and 2b. The decay of HPMTF and MTF were used to estimate their reaction rate coefficients with OH.

270



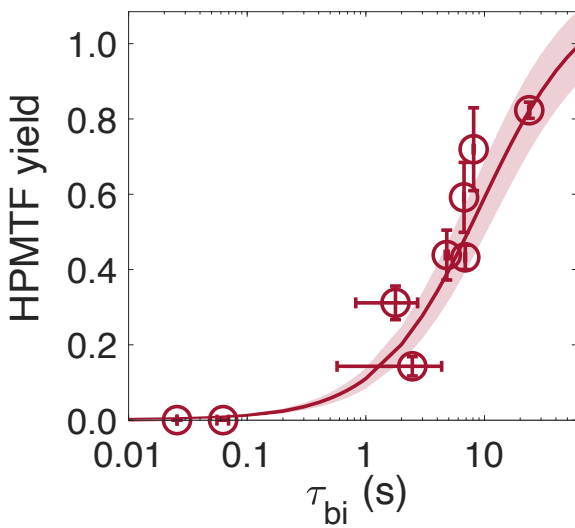
271

272
273
274
275
276

Figure S6: Time series of (a) NO and (b) N₂O₅ in Experiment 3. The initial concentration of NO of every injection was constrained by the measurements and the remaining decay was predicted by the model (there were large measurement uncertainties in the sub-ppb range in the NO-NO₂-NO_x Analyzer). Concentration of N₂O₅ is from the model. Yellow stripes indicate the 10-minute periods used in k_{isom} estimation (Figure 3a). Increases in N₂O₅ can lead to interferences in the HPMTF-¹²C₂ signal in the I-CIMS spectra.

277

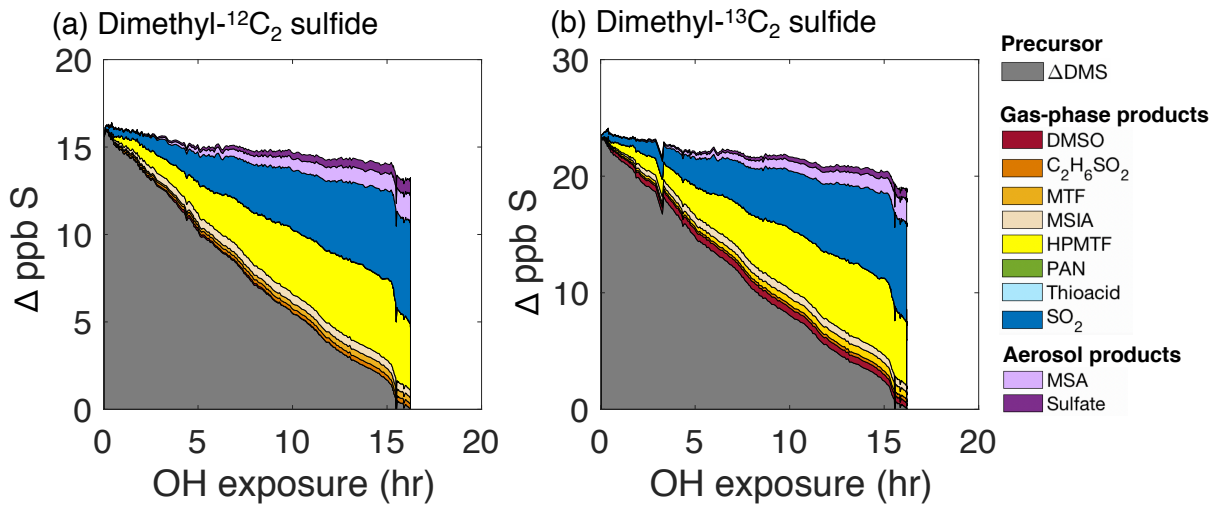
278



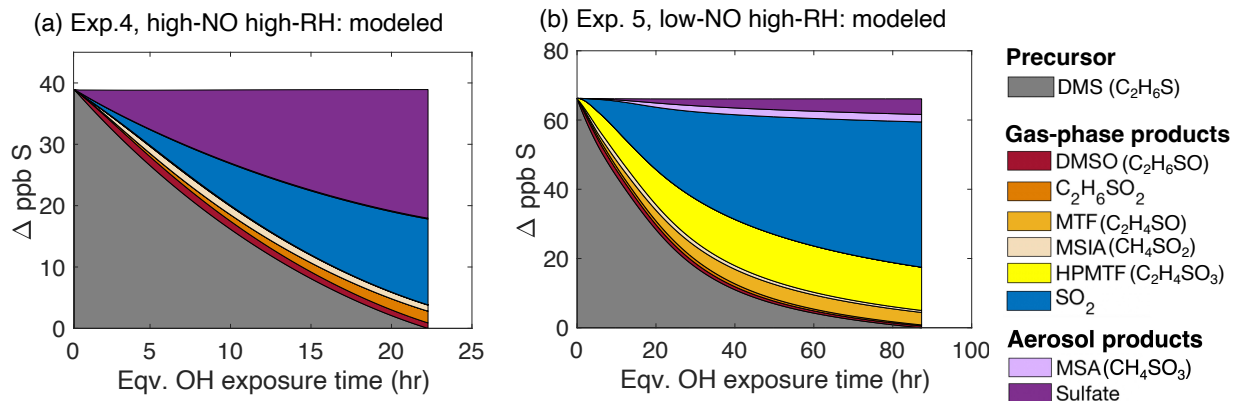
279

280
281
282

Figure S7: Yields of HPMTF as a function of RO₂ bimolecular lifetime without considering HPMTF + OH for DMS-¹³C₂.



283
284 Figure S8: Measurements of total sulfur distribution of (a) DMS-¹²C₂ and (b) DMS-¹³C₂ in Exp. 3.
285



286
287 Figure S9: (a) Modeled product distribution of Exp. 4. (b) Modeled product distribution of Exp. 5.
288

289 References:

290 Barnes, I., Hjorth, J. and Mihalopoulos, N.: Dimethyl sulfide and dimethyl sulfoxide and their
291 oxidation in the atmosphere, *Chem. Rev.*, 106(3), 940–975, doi:10.1021/cr020529+, 2006.

292 Capouet, M., and J-F. Müller.: A group contribution method for estimating the vapour pressures
293 of α -pinene oxidation products, *Atmos. Chem. Phys* 6(6), 1455–1467, doi:10.5194/acp-6-1445-
294 2006, 2006.

295 Compernolle S., Ceulemans, K., Müller, J.F.: EVAPORATION: a new vapor pressure estimation
296 method for organic molecules including non-additivity and intramolecular interactions, *Atmos.*
297 *Chem. Phys.*, 11 (18), 9431-9450, 2011, doi:10.5194/acp-11-9431-2011

298 Guo, H., Campuzano-Jost, P., Nault, B. A., Day, D. A., Schroder, J. C., Kim, D., Dibb, J. E.,
299 Dollner, M., Weinzierl, B. and Jimenez, J. L.: The importance of size ranges in aerosol instrument
300 intercomparisons: a case study for the Atmospheric Tomography Mission, *Atmos. Meas. Tech.*,
301 14(3631–3655), 2021.

302 Hodshire, A. L., Campuzano-Jost, P., Kodros, J. K., Croft, B., Nault, B. A., Schroder, J. C.,
303 Jimenez, J. L. and Pierce, J. R.: The potential role of methanesulfonic acid (MSA) in aerosol
304 formation and growth and the associated radiative forcings, *Atmos. Chem. Phys.*, 19(5), 3137–
305 3160, doi:10.5194/acp-19-3137-2019, 2019.

306 Huang, S., Poulain, L., Pinxteren, D. Van, Pinxteren, M. Van, Wu, Z., Herrmann, H. and
307 Wiedensohler, A.: Latitudinal and Seasonal Distribution of Particulate MSA over the Atlantic
308 using a Validated Quantification Method with HR-ToF-AMS, , doi:10.1021/acs.est.6b03186,
309 2017.

310 Isaacman-Vanwertz, G., Massoli, P., O'Brien, R., Lim, C., Franklin, J. P., Moss, J. A., Hunter, J.
311 F., Nowak, J. B., Canagaratna, M. R., Misztal, P. K., Arata, C., Roscioli, J. R., Herndon, S. T.,
312 Onasch, T. B., Lambe, A. T., Jayne, J. T., Su, L., Knopf, D. A., Goldstein, A. H., Worsnop, D. R.
313 and Kroll, J. H.: Chemical evolution of atmospheric organic carbon over multiple generations of
314 oxidation, *Nat. Chem.*, 10(4), 462–468, doi:10.1038/s41557-018-0002-2, 2018.

315 Jenkin, M. E., Saunders, S. M. and Pilling, M. J.: The tropospheric degradation of volatile organic
316 compounds: a protocol for mechanism development, *Atmos. Environ.*, 31(1), 81–104, 1997.

317 Krechmer, E. J., Lopez-Hilfiker, F., Koss, A., Hutterli, M., Stoermer, C., Deming, B., Kimmel, J.,
318 Warneke, C., Holzinger, R., Jayne, J., Worsnop, D., Fuhrer, K., Gonin, M. and Gouw, J. De:
319 Evaluation of a new reagent-ion source and focusing ion-molecule reactor for use in proton-
320 transfer-reaction mass spectrometry, *Anal. Chem.*, 90, 12011–12018,
321 doi:10.1021/acs.analchem.8b02641, 2018.

322 Krechmer, E. J., Pagonis, D., Ziemann, P. J., Jimenez, J. L.: Quantification of gas-wall partitioning
323 in Teflon environmental chambers using rapid bursts of low-volatility oxidized species generated
324 in situ, *Environ. Sci. Technol.*, 50 (11), 5757–5765, doi:10.1021/acs.est/6b00606, 2016.

325 Lopez-Hilfiker, F. D., Iyer, S., Mohr, C., Lee, B. H., D'ambro, E. L., Kurtén, T. and Thornton, J.
326 A.: Constraining the sensitivity of iodide adduct chemical ionization mass spectrometry to
327 multifunctional organic molecules using the collision limit and thermodynamic stability of iodide
328 ion adducts, *Atmos. Meas. Tech.*, 9(4), 1505–1512, doi:10.5194/amt-9-1505-2016, 2016.

329 McManus, J.B., Zahniser, M.S., Nelson, D.D., McGovern, R.M., Agnese, M. and Brown, W.F.:
330 Compact Quantum Cascade Laser Instrument for High Precision Trace Gas Measurements.
331 In Optical Instrumentation for Energy and Environmental Applications (p. EThC2). Optica
332 Publishing Group, 2011, November.

333 McManus, J.B., Kebabian, P.L. and Zahniser, M.S.: Astigmatic mirror multipass absorption cells
334 for long-path-length spectroscopy. *Applied Optics*, 34(18), 3336–3348, 1995.

335 Novak, G. A., Fite, C. H., Holmes, C. D., Veres, P. R., Neuman, J. A., Faloona, I., Thornton, J. A.,
336 Wolfe, G. M., Vermeuel, M. P., Jernigan, C. M., Peischl, J., Ryerson, T. B., Thompson, C. R.,
337 Bourgeois, I., Warneke, C., Gkatzelis, G. I., Coggon, M. M., Sekimoto, K., Bui, T. P., Dean-Day,
338 J., Diskin, G. S., DiGangi, J. P., Nowak, J. B., Moore, R. H., Wiggins, E. B., Winstead, E. L.,
339 Robinson, C., Thornhill, K. L., Sanchez, K. J., Hall, S. R., Ullmann, K., Dollner, M., Weinzierl,
340 B., Blake, D. R. and Bertram, T. H.: Rapid cloud removal of dimethyl sulfide oxidation products
341 limits SO₂ and cloud condensation nuclei production in the marine atmosphere, *Proc. Natl. Acad.*
342 *Sci.*, 118(42), e2110472118, doi:10.1073/PNAS.2110472118, 2021.

343 Pankow, J. F., and Asher, W. E.: SIMPOL. 1: a simple group contribution method for predicting
344 vapor pressures and enthalpies of vaporization of multifunctional organic compounds, *Atmos*
345 *Chem and Phys*, 8(10), 2773-2796, doi:10.5194/acp-8-2772-2008, 2008.

346 Saunders, S. M., Jenkin, M. E., Derwent, R. G. and Pilling, M. J.: Protocol for the development of
347 the Master Chemical Mechanism, MCM v3 (Part A): Tropospheric degradation of non-aromatic
348 volatile organic compounds, *Atmos. Chem. Phys.*, 3(1), 161–180, doi:10.5194/acp-3-161-2003,
349 2003.

350 Vermeuel, M. P., Novak, G. A., Jernigan, C. M. and Bertram, T. H.: Diel Profile of
351 Hydroperoxymethyl Thioformate: Evidence for Surface Deposition and Multiphase Chemistry,
352 *Environ. Sci. Technol.*, 54(19), 12521–12529, doi:10.1021/acs.est.0c04323, 2020.

353 Wang, N., Jorga, S. D., Pierce, J. R., Donahue, N. M. and Pandis, S. N.: Particle wall-loss
354 correction methods in smog chamber experiments, *Atmos. Meas. Tech.*, 11, 6577–6588, 2018.

355 Wu, R., Wang, S. and Wang, L.: New mechanism for the atmospheric oxidation of dimethyl
356 sulfide. The importance of intramolecular hydrogen shift in a $\text{CH}_3\text{SCH}_2\text{OO}$ radical, *J. Phys. Chem.*
357 A, 119(1), 112–117, doi:10.1021/jp511616j, 2015.

358 Ye, Q., Goss, M. B., Isaacman-Vanwertz, G., Zaytsev, A., Massoli, P., Lim, C., Croteau, P.,
359 Canagaratna, M., Knopf, D. A., Keutsch, F. N., Heald, C. L. and Kroll, J. H.: Organic Sulfur
360 Products and Peroxy Radical Isomerization in the OH Oxidation of Dimethyl Sulfide, *ACS Earth*
361 *Sp. Chem.*, 5(8), 2013–2020, doi:10.1021/acsearthspacechem.1c00108, 2021.

362 Zaytsev, A., Breitenlechner, M., Koss, A. R., Lim, C. Y., Rowe, J. C., Kroll, J. H. and Keutsch, F.
363 N.: Using collision-induced dissociation to constrain sensitivity of ammonia chemical ionization
364 mass spectrometry (NH_4^+ CIMS) to oxygenated volatile organic compounds, *Atmos. Meas. Tech.*,
365 12(3), 1861–1870, doi:10.5194/amt-12-1861-2019, 2019.

366 Zorn, S. R., Drewnick, F., Schott, M., Hoffmann, T. and Borrmann, S.: Characterization of the
367 South Atlantic marine boundary layer aerosol using an aerodyne aerosol mass spectrometer,
368 *Atmos. Chem. Phys.*, 8, 4711–4728, 2008.

369